Sixth International Symposium on Marine Propulsors
smp'19, Rome, Italy, May 2019

Prediction of the Propeller Performance at Different Reynolds Number Regimes with RANS

J. Baltazar[1], D. Rijpkema[2], J.A.C. Falcão de Campos[1]

[1]Instituto Superior Técnico (IST), Universidade de Lisboa, Portugal
[2]Maritime Research Institute Netherlands (MARIN), Wageningen, the Netherlands

ABSTRACT

In this study, a Reynolds averaged Navier-Stokes solver is used for prediction of the propeller performance in open-water conditions at different Reynolds numbers ranging from 10^4 to 10^7. The $k-\omega$ SST turbulence model and the $\gamma-\tilde{\mathrm{Re}}_{\theta_t}$ transition model are utilised and results compared for a conventional marine propeller. First, the selection of the turbulence inlet quantities for different flow regimes is discussed. Then, an analysis of the iterative and discretisation errors is made. This work is followed by an investigation of the predicted propeller flow and wake field at variable Reynolds numbers. Finally, the propeller scale-effects and the influence of the turbulence and transition models on the performance prediction are discussed. The variation of the flow regime showed an increase in thrust and decrease in torque for increasing Reynolds number. From the comparison between the turbulence model and the transition model, different flow solutions are obtained for the Reynolds numbers between 10^5 and 10^6.

Keywords

Marine Propeller, Flow Regimes, RANS Equations, Turbulence and Transition Models.

1 INTRODUCTION

The prediction of propeller performance in full-scale is usually based on model-scale experiments carried out in a towing tank or cavitation tunnel. Then, the full-scale performance is subsequently determined using simple extrapolation procedures from the model-scale results (International Towing Tank Conference 2017).

Complementary to model tests, Reynolds-averaged Navier-Stokes (RANS) solvers are increasingly being used for the prediction of the propeller performance and quantification of the scale-effects. A large variety of studies have been presented for open propellers (Stanier 1998, Krasilnikov et al. 2009, Sánchez-Caja et al. 2014, Rijpkema et al. 2015) and ducted propellers (Abdel-Maksoud and Heinke 2002, Rijpkema and Vaz 2011, Bhattacharyya et al. 2016).

For the prediction of the scale-effects with RANS, the most common choice for turbulence modelling has been the Shear-Stress Transport (SST) two-equation linear eddy-viscosity model (Menter 1994, Menter et al. 2003). It is known that this turbulence model predicts well the viscous flow for fully developed turbulent flows, but it is not able to model the transition from laminar to turbulent flow. Eça and Hoekstra (2008) tested, for the case of a flat plate, several turbulence models including the $k-\omega$ two-equation model proposed by Wilcox (1988) and its SST variant. Results showed that transition occurs at a too low Reynolds number, and only a small region of laminar flow is obtained at the leading edge of the plate.

The flow around propellers in full-scale is assumed to be fully-turbulent. However, at model-scale different flow patterns may occur simultaneously: laminar flow, transition to turbulent, and turbulent flow. Additionally, flow separation may occur at model-scale, which is not present at full-scale.

In order to take into account the effect of flow transition at model-scale in the computation of the scale-effects, the $\gamma-\tilde{\mathrm{Re}}_{\theta_t}$ correlation-based transition model proposed by Langtry and Menter (2009) is selected. In Baltazar et al. (2018), simulations obtained with the $k-\omega$ SST turbulence model (Menter et al. 2003) and $\gamma-\tilde{\mathrm{Re}}_{\theta_t}$ transition model (Langtry and Menter 2009) were compared to experimental paint-tests carried out at model-scale for two marine propellers. From this comparison and depending on the turbulence inlet quantities, an improvement in the flow pattern was achieved with the $\gamma-\tilde{\mathrm{Re}}_{\theta_t}$ transition model.

Therefore, it was decided to use the $\gamma-\tilde{\mathrm{Re}}_{\theta_t}$ transition model (Langtry and Menter 2009) for the prediction of the viscous flow at different Reynolds number regimes and to compare with the $k-\omega$ SST turbulence model predictions (Menter et al. 2003). In this paper, viscous flow calculations using a RANS method are presented for a marine propeller in open-water conditions at different Reynolds numbers ranging from 10^4 to 10^7. The paper is organised as follows: the mathematical model including the turbulence and transition models are given in Section 2; the propeller geometry, flow solver, and numerical set-up are described in Section 3; results are presented and discussed in Section 4; the paper ends with the main conclusions of this study.

2 MATHEMATICAL MODEL

2.1 RANS Equations

The flow simulation is based on the solution of the RANS equations. We introduce two reference frames: an inertial earth-fixed reference frame (X, Y, Z) or X_i with $(i = 1, 2, 3)$, and a non-inertial propeller-fixed reference frame (x, y, z) or x_i, which is rotating with constant angular velocity Ω. The mean velocity vector defined in respect to the earth-fixed reference frame (the so-called absolute velocity) is given by U_i, and defined in respect to the propeller-fixed reference, also known as the relative velocity, is given by V_i. If we consider that the propeller is operating in open-water conditions, then the flow is statistically steady in the propeller-fixed reference frame.

Assuming that the fluid is incompressible, the RANS (continuity and momentum) equations written in the propeller-fixed reference frame x_i and considering as the unknown the mean velocity in respect to the earth-fixed reference frame U_i, take the form

$$\begin{aligned}&\frac{\partial U_i}{\partial x_i} = 0,\\ &\rho\frac{\partial (V_j U_i)}{\partial x_j} + \rho\varepsilon_{ijk}\Omega_j U_k = \\ &\qquad -\frac{\partial P}{\partial x_i} + \frac{\partial}{\partial x_j}\left[(\mu+\mu_t)\left(\frac{\partial U_i}{\partial x_j}+\frac{\partial U_j}{\partial x_i}\right)\right],\end{aligned} \tag{1}$$

where ρ is the fluid density, μ the fluid viscosity, μ_t the eddy-viscosity and ε the Levi-Civita symbol. The modified pressure is given by $P = p + 2/3\rho k$, where p is the static pressure with the hydrostatic pressure as the reference, and k the turbulence kinetic energy. In this work, the Reynolds stresses are determined from the turbulence and transition models, which are based on the Boussinesq eddy-viscosity hypothesis (Schmitt 2007). We note that in this formulation, the Coriolis and centripetal accelerations are simplified into a single term $\varepsilon_{ijk}\Omega_j U_k$, which reduces the number of source terms of the momentum equation.

2.2 $k-\omega$ SST Model

The SST two-equation turbulence model proposed by Menter et al. (2003) is selected to solve the transport equations for the turbulence kinetic energy k:

$$\rho\frac{\partial (V_j k)}{\partial x_j} = P_k - \beta^*\rho\omega k + \frac{\partial}{\partial x_j}\left(\mu_k\frac{\partial k}{\partial x_j}\right), \tag{2}$$

and for the turbulence dissipation rate ω:

$$\rho\frac{\partial (V_j \omega)}{\partial x_j} = P_\omega - \beta\rho\omega^2 + \frac{\partial}{\partial x_j}\left(\mu_\omega\frac{\partial \omega}{\partial x_j}\right) + \frac{\sigma_d}{\omega}\frac{\partial k}{\partial x_j}\frac{\partial \omega}{\partial x_j}, \tag{3}$$

where P_k and P_ω are the production terms of the turbulence kinetic energy and turbulence dissipation rate, respectively. The SST formulation is a combination of two of the most commonly-used two-equation models. The $k-\omega$ model (Wilcox 1988) is used in the sub- and log-layer and gradually switches to the $k-\epsilon$ model (Jones and Launder 1972) in the wake region of the boundary layer and in free shear flows. The blending between the two models is made via the F_1 function. In this model, the coefficients are:

$$\begin{aligned}&\beta^* = 0.09,\\ &\beta = 0.0828 - 0.0078F_1,\\ &\mu_k = \mu + (1-0.15F_1)\mu_t,\\ &\mu_\omega = \mu + (0.856 - 0.356F_1)\mu_t,\\ &\sigma_d = 1.712(1-F_1)\rho.\end{aligned} \tag{4}$$

The eddy-viscosity μ_t is defined as follows:

$$\mu_t = \frac{\rho a_1 k}{\max(a_1\omega, S\,F_2)}, \tag{5}$$

where S is the strain rate magnitude, F_2 a second blending function and $a_1 = 0.31$. The definitions of the blending functions F_1 and F_2 may be found in Menter et al. (2003).

2.3 $\gamma - \tilde{\mathrm{Re}}_{\theta_t}$ Correlation-Based Transition Model

In this work, the $\gamma - \tilde{\mathrm{Re}}_{\theta_t}$ correlation-based transition model proposed by Langtry and Menter (2009) is selected for transition prediction. This transition model contains two transport equations and accounts for transition due to free-stream turbulence intensity, pressure gradients and separation. One is a transport equation for intermittency γ:

$$\rho\frac{\partial (V_j \gamma)}{\partial x_j} = P_\gamma - E_\gamma + \frac{\partial}{\partial x_j}\left[\left(\mu + \frac{\mu_t}{\sigma_f}\right)\frac{\partial \gamma}{\partial x_j}\right], \tag{6}$$

where P_γ and E_γ are the production and relaminarisation terms, respectively. The second one is a transport equation for the local transition onset momentum thickness Reynolds number $\tilde{\mathrm{Re}}_{\theta_t}$:

$$\rho\frac{\partial (V_j \tilde{\mathrm{Re}}_{\theta_t})}{\partial x_j} = P_{\theta t} + \frac{\partial}{\partial x_j}\left[\sigma_{\theta t}(\mu+\mu_t)\frac{\partial \tilde{\mathrm{Re}}_{\theta_t}}{\partial x_j}\right], \tag{7}$$

which only includes a production term $P_{\theta t}$. The terms P_γ, E_γ and $P_{\theta t}$ and the constants σ_f and $\sigma_{\theta t}$ are given in Langtry and Menter (2009).

This model is also sometimes known as the $\gamma - \tilde{\mathrm{Re}}_{\theta_t} - \mathrm{SST}$ model, because it makes use of the equations for γ and $\tilde{\mathrm{Re}}_{\theta_t}$, in addition to the k and ω equations of the SST turbulence model (Menter et al. 2003). Therefore, this model corresponds to a four-equation transition SST turbulence model. We note that the definitions of production and dissipation terms of the k-equation, and the blending function F_1 change due to the coupling with the $\gamma - \tilde{\mathrm{Re}}_{\theta_t}$ model.

2.4 Inflow Turbulence Quantities

In this section the selection of the inlet turbulence quantities for the $k-\omega$ SST turbulence and $\gamma - \tilde{\mathrm{Re}}_{\theta_t}$ transition models is analysed. The strong dependence of the $\gamma - \tilde{\mathrm{Re}}_{\theta_t}$ transition model on the turbulence inlet quantities has been

discussed earlier, see Eça et al. (2016). In a previous study (Baltazar et al. 2018), experimental streamlines obtained from paint-tests carried out at model-scale were used to obtain reference values for the prediction of the transition location. For the $k-\omega$ SST turbulence model, standard values, i.e. $\mathrm{Tu} = 1.0\%$ and $\mu_t/\mu = 1$, were assumed as the initial and inlet turbulence quantities. The turbulence intensity at the inlet, in percent, is related to k by the relation $\mathrm{Tu} = 100\sqrt{2k/(3U_{\mathrm{inlet}}^2)}$, where U_{inlet} is the fluid velocity at the inlet. For the $\gamma - \tilde{\mathrm{Re}}_{\theta_t}$ transition model, initial and inlet values equal to $\mathrm{Tu} = 2.5\%$ and $\mu_t/\mu = 500$ were considered, since it corresponds to the best qualitative agreement between the calculated limiting streamlines and the paint-tests carried out at $\mathrm{Re} = 5{\times}10^5$. These values also take into account the decay of the turbulence quantities along the streamwise direction due to the distance between the inlet boundary and the propeller.

In the present study, a criterion considering the different Reynolds number regimes needs to be found for the initial and inlet turbulence quantities. If we consider the case of a uniform flow U_∞, then the decay of the turbulence quantities is given by the following analytical solutions (Spalart and Rumsey 2007), written in the dimensionless form, of the transport equations for k and ω:

$$k^* = k^*_{\mathrm{inlet}} \left(1 + \beta(x^* - x^*_{\mathrm{inlet}}) \frac{k^*_{\mathrm{inlet}}}{(\mu_{t\mathrm{inlet}}/\mu)} \mathrm{Re}\right)^{-\beta^*/\beta},$$
$$\omega^* = \omega^*_{\mathrm{inlet}} \left(1 + \beta(x^* - x^*_{\mathrm{inlet}}) \frac{k^*_{\mathrm{inlet}}}{(\mu_{t\mathrm{inlet}}/\mu)} \mathrm{Re}\right)^{-1}, \tag{8}$$

where $x^* = x/L_{\mathrm{ref}}$, $k^* = k/U_\infty^2$, $\omega^* = \omega L_{\mathrm{ref}}/U_\infty$, k_{inlet} and ω_{inlet} are the values specified at the inlet, and L_{ref} is a reference length. In this case, the Reynolds number is defined as $\mathrm{Re} = \rho U_\infty L_{\mathrm{ref}}/\mu$. Equation (8) shows a strong decay, especially for the turbulence kinetic energy k; the power is about -1.087. We note that for higher Reynolds numbers, larger values of the eddy-viscosity ratio are needed to control the decay rate of the turbulence quantities.

In the present study, the same value of the inlet turbulence intensity, as defined in Baltazar et al. (2018), is assumed for all Reynolds numbers and the eddy-viscosity ratio is adjusted according to Equation (8) to maintain the same decay rate from the simulations at model-scale ($\mathrm{Re} = 5{\times}10^5$). In this sense, the inlet eddy-viscosity ratio is specified by:

$$\frac{\mu_{t\mathrm{inlet}}}{\mu} = \frac{\mathrm{Re}}{5 \times 10^5} \cdot \left.\frac{\mu_{t\mathrm{inlet}}}{\mu}\right|_{\mathrm{Re}=5\times10^5}. \tag{9}$$

Table 1 presents the initial and inlet turbulence quantities assumed for the simulations at the various Reynolds numbers. We note that large values of the eddy-viscosity ratio are obtained for the higher Reynolds numbers and, at this point, it is not known how these non-realistic eddy-viscosity ratios influence the numerical solutions.

Table 1: Inlet turbulence quantities for the calculations at different Reynolds number.

Model	$k-\omega$ SST		$\gamma - \tilde{\mathrm{Re}}_{\theta_t}$	
Re	Tu	μ_t/μ	Tu	μ_t/μ
$1{\times}10^4$	1.0%	0.02	2.5%	10
$5{\times}10^4$	1.0%	0.1	2.5%	50
$1{\times}10^5$	1.0%	0.2	2.5%	100
$5{\times}10^5$	1.0%	1	2.5%	500
$1{\times}10^6$	1.0%	2	2.5%	1000
$5{\times}10^6$	1.0%	10	2.5%	5000
$1{\times}10^7$	1.0%	20	2.5%	10000

After setting the initial and inlet turbulence quantities, Equation (9), the contribution of the Reynolds stresses as function of the Reynolds number to the momentum balance can be analysed. If we write the momentum equation, Equation (1), in the dimensionless form by taking $x^* = x/L_{\mathrm{ref}}$, $U^* = U/U_\infty$, $V^* = V/U_\infty$, $\Omega* = \Omega L_{\mathrm{ref}}/U_\infty$ and $P^* = P/(\rho U_\infty^2)$, we obtain:

$$\frac{\partial(V_j^* U_i^*)}{\partial x_j^*} + \varepsilon_{ijk}\Omega_j^* U_k^* = - \frac{\partial P^*}{\partial x_i^*} + \frac{\partial}{\partial x_j^*}\left[\frac{1}{\mathrm{Re}}\left(1 + \frac{\mu_t}{\mu}\right)\left(\frac{\partial U_i^*}{\partial x_j^*} + \frac{\partial U_j^*}{\partial x_i^*}\right)\right], \tag{10}$$

By combining Equations (9) and (10), we observe that the contribution of the Reynolds stresses to the momentum balance as function of the Reynolds number is maintained.

3 SOLVER, PROPELLER, GRIDS, DOMAIN AND BOUNDARY CONDITIONS

3.1 Flow Solver

For the flow simulations, the RANS equations are discretised using a finite-volume approach with cell-centred collocated variables. A strong-conservation form and a pressure-correction equation based on the SIMPLE algorithm is used to ensure mass conservation. The implementation is face-based, which allows grids with elements consisting of an arbitrary number of faces and hanging nodes. A second-order convection scheme (QUICK) is used for the momentum equations and a first-order upwind scheme is used for the $k-\omega$ SST turbulence model and the $\gamma - \tilde{\mathrm{Re}}_{\theta_t}$ transition model. The RANS equations are solved using the ReFRESCO code, which is targeted for hydrodynamic applications (www.refresco.org). ReFRESCO is currently being developed within a cooperation led by MARIN. In this study, ReFRESCO version 2.1 is used.

3.2 Propeller Geometry

The marine propeller S6368 is considered in the present study. The main particulars are listed in Table 2. A set

Table 2: Overview of propeller particulars with R denoting the propeller radius.

Diameter D [m]	0.2714
Chord length at $r = 0.7R$ [m]	0.0694
Number of blades	4
Pitch ratio P/D at $r = 0.7R$	0.757
Blade-area ratio A_E/A_0	0.464

of experiments has been carried out at MARIN and is reported in Jonk and Willemsen (1994). This propeller was also used by Boorsma (2000) to study the differences in the propeller performance due to leading-edge roughness.

3.3 Grid Sets

Two series of six nearly-geometrically similar multi-block structured grids are generated using the commercial grid generation package GridPro (www.gridpro.com). The first grid series is used for the calculations at the Reynolds numbers from $1{\times}10^4$ to $5{\times}10^5$. The grids range from 1 to 35 million cells. The second grid series is used for the calculations at the Reynolds numbers from $1{\times}10^6$ to $1{\times}10^7$. The grids range from 1 to 39 million cells. Table 3 presents the number of cells in the volume and on a single blade, and the maximum and mean dimensionless wall distance of the first cell height y^+ at the Reynolds numbers $1{\times}10^4$, $5{\times}10^5$ and $1{\times}10^7$. The y^+ values correspond to the calculations using the $k-\omega$ SST turbulence model (Menter et al. 2003) at design condition. The differences between the two grid series are due to the grid space weighting in the boundary-layer region in order to obtain a $y^+ < 1$ for all Reynolds number regimes. Therefore, the boundary layer is fully resolved and no wall functions are used. An overview of the grid with 8 million cells is presented in Figure 1.

Table 3: Overview of the grid sizes and number of cell faces on a single blade. Maximum and mean y^+ at the Reynolds numbers $\mathrm{Re} = 1{\times}10^4$, $5{\times}10^5$ and $1{\times}10^7$.

Volume	1.0M	2.2M	4.3M	8.0M	17.8M	34.8M
Blade	4k	6k	10k	15k	25k	39k
$\mathrm{Re} = 1{\times}10^4$						
$\max y^+$	0.04	0.04	0.03	0.03	0.02	0.02
mean y^+	0.01	0.01	0.01	0.00	0.00	0.00
$\mathrm{Re} = 5{\times}10^5$						
$\max y^+$	0.74	0.67	0.54	0.45	0.36	0.31
mean y^+	0.23	0.18	0.13	0.11	0.08	0.06
Volume	1.4M	3.2M	6.1M	11.4M	25.0M	39.0M
Blade	4k	6k	10k	15k	25k	39k
$\mathrm{Re} = 1{\times}10^7$						
$\max y^+$	0.34	0.26	0.20	0.16	0.12	0.10
mean y^+	0.10	0.08	0.06	0.05	0.04	0.03

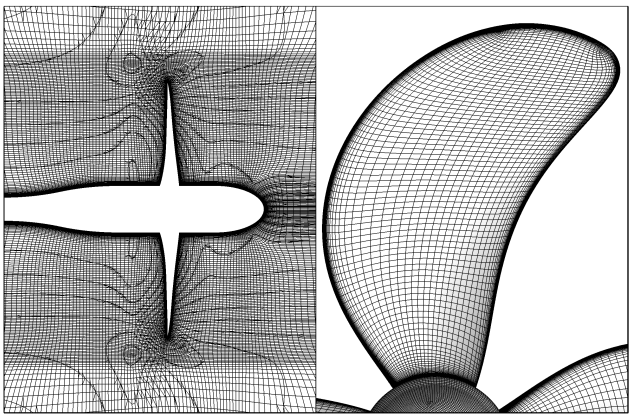

Figure 1: Overview of the grid around propeller and blades. Grid with 8.0M cells.

3.4 Computational Domain and Boundary Conditions

In the simulations a cylindrical domain is considered, where the inlet, the outlet and the outer boundary are located five propeller diameters from the propeller origin. At the inlet the velocity, and the turbulence intensity and eddy-viscosity ratio depending on the turbulence model or transition model are prescribed, see Table 1. For the outer boundary a constant pressure is specified. At the outlet an outflow condition of zero downstream gradient is used. On the propeller blades and hub a no-slip boundary condition is used with zero velocity in the rotating reference frame.

4 RESULTS

4.1 General

Results are presented for the marine propeller S6368 in open-water conditions. The operating conditions are defined by the advance coefficient $J = U/(nD)$, where U is the propeller advance speed, D the propeller diameter and $n = \Omega/(2\pi)$ is the rotation rate in rps. The open-water characteristics are expressed by the thrust coefficient $K_T = T/(\rho n^2 D^4)$, torque coefficient $K_Q = Q/(\rho n^2 D^5)$ and open-water efficiency $\eta_0 = JK_T/(2\pi K_Q)$, where T is the propeller thrust and Q the propeller torque. Other useful quantity is the friction coefficient $C_f = \tau_w/(1/2\rho U^2)$, where τ_w is the local wall shear stress.

Simulations are carried out at $J = 0.568$ (near design condition) for a range of Reynolds numbers between $1{\times}10^4$ to $1{\times}10^7$, which cover different flow regimes, i.e. from fully laminar to turbulent flow. The Reynolds number is defined based on the propeller blade chord length at $0.7R$, $c_{0.7R}$, and the resulting onset velocity at that radius:

$$\mathrm{Re} = \frac{\rho c_{0.7R}\sqrt{U^2 + (n\pi 0.7D)^2}}{\mu}. \qquad (11)$$

For the flow computations, the same geometrical scale is used as for the model-scale simulations, i.e. $\mathrm{Re} = 5{\times}10^5$, and the variation of the Reynolds number is achieved by adapting the propeller rotation rate n.

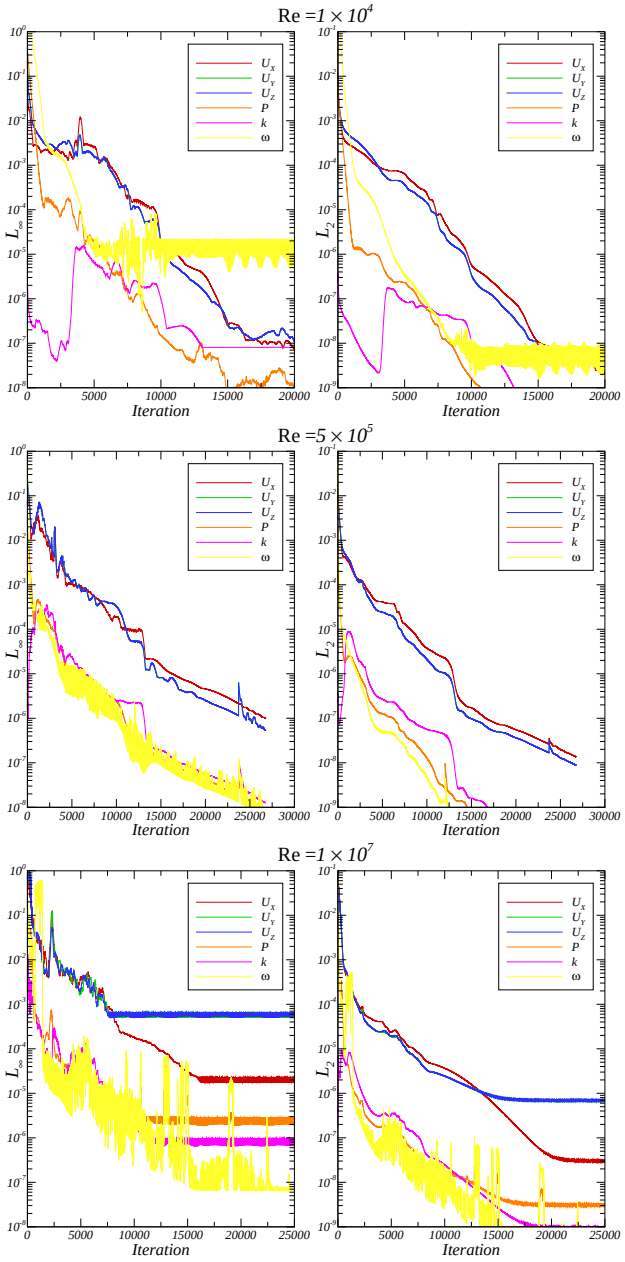

Figure 2: L_∞ (left) and L_2 (right) iterative convergence at $J = 0.568$ using the $k-\omega$ SST turbulence model. $\mathrm{Re} = 1{\times}10^4$ (top), $5{\times}10^5$ (middle) and $1{\times}10^7$ (bottom).

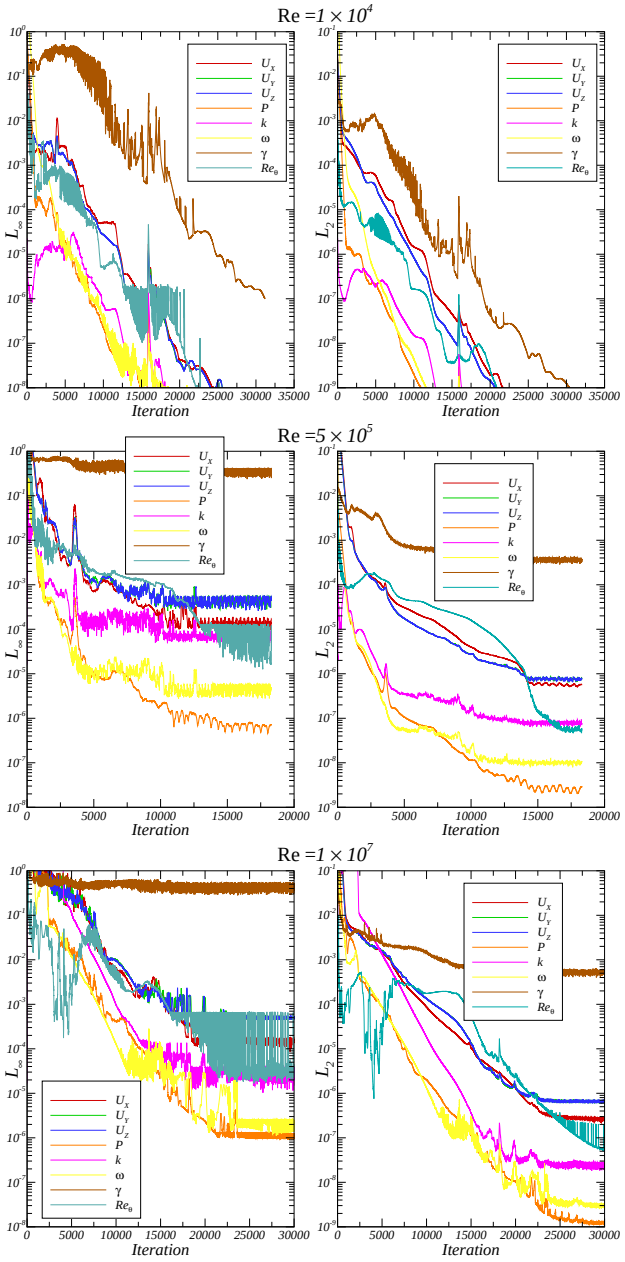

Figure 3: L_∞ (left) and L_2 (right) iterative convergence at $J = 0.568$ using the $\gamma - \tilde{\mathrm{Re}}_{\theta_t}$ transition model. $\mathrm{Re} = 1{\times}10^4$ (top), $5{\times}10^5$ (middle) and $1{\times}10^7$ (bottom).

4.2 Estimation of Numerical Errors

In this section the numerical errors that occur in the calculations are analysed. The numerical errors involved in every computing simulation can be divided into three types (Oberkampf and Roy 2010): round-off error, iterative error and discretisation error.

Since double-precision is used in the present calculations, the round-of error is neglected. The iterative error, which occurs due to the iterative solution of the transport equations, is monitored with the infinity norm L_∞ and L_2 norm of the residuals,

$$L_\infty(\phi) = \max|\mathrm{res}(\phi_i)|, \quad 1 \le i \le N_{\mathrm{cells}},$$
$$L_2(\phi) = \sqrt{\sum_{i=1}^{N_{\mathrm{cells}}} \mathrm{res}^2(\phi_i) \Big/ N_{\mathrm{cells}}} \tag{12}$$

in which $\mathrm{res}(\phi_i)$ stands for the residual of any local flow quantity and N_{cells} is the total number of grid cells. The iterative convergence at $J = 0.568$ using the $k-\omega$ SST turbulence model and $\gamma - \tilde{\mathrm{Re}}_{\theta_t}$ transition model is presented in Figures 2 and 3, respectively. The local flow quantities considered are the Cartesian components of the flow velocity $U_{X,Y,Z}$, the modified static pressure P, the turbulence kinetic energy k, the specific turbulence dissipation

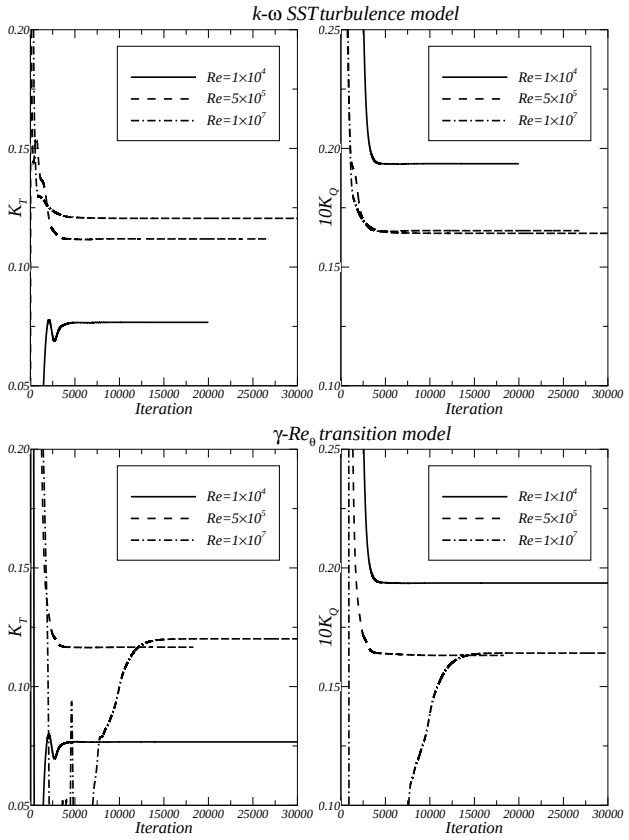

Figure 4: Iterative convergence of K_T (left) and $10K_Q$ (right) at $J = 0.568$ using the $k-\omega$ SST turbulence model (top) and $\gamma - \tilde{\mathrm{Re}}_{\theta_t}$ transition model (bottom).

rate ω, the intermittency γ and the local transition onset momentum thickness Reynolds number $\tilde{\mathrm{Re}}_{\theta_t}$. The results refer to the grids with 17.8 million cells, for $\mathrm{Re} = 1{\times}10^4$ and $5{\times}10^5$, and 11.4 million cells, for $\mathrm{Re} = 1{\times}10^7$. In this study a convergence criterion of 10^{-6} is adopted for the L_∞ and L_2 norms of the local variables. The analysis of the results for $\mathrm{Re} = 1{\times}10^4$ show that this convergence criterion is achieved for all quantities, with the exception of the turbulence dissipation rate ω in the simulation using the $k-\omega$ SST turbulence model, where the residual stagnates at approximately 10^{-5}. For the Reynolds number $5{\times}10^5$, iterative convergence is only obtained with the $k-\omega$ SST turbulence model. With the $\gamma - \tilde{\mathrm{Re}}_{\theta_t}$ transition model, convergence of the flow quantities is difficult to achieve, especially for intermittency γ, where the residual stagnates between 0.1 and 1. For the Reynolds number $1{\times}10^7$, a similar behaviour is observed for both models, since the residuals stagnate with the number of iterations. We note that for the simulations carried out with the $k-\omega$ SST turbulence model, the L_2 norm of the residuals is lower than 10^{-6} for all flow quantities. This result shows that the maximum residuals have a minor contribution to the global iterative error and it occurs locally at the trailing-edge near the blade tip. With the $\gamma - \tilde{\mathrm{Re}}_{\theta_t}$ transition model, the large residuals observed in the intermittency occur at the blade mid-chord and leading-edge for $\mathrm{Re} = 5{\times}10^5$ and $1{\times}10^7$, respectively. These locations coincide with the predicted transition region, suggesting that denser grids may be needed in these regions. With the exception of the intermittency, L_2 norm of the residuals lower than 10^{-6} is obtained for the remaining flow quantities. In addition, the iterative convergence of the propeller thrust and torque coefficients is plotted in Figure 4. Convergence is obtained for all cases, preceding the criterion of 10^{-6} and the stagnation of the residuals. These results suggest a negligible effect of the iterative error on the propeller forces.

The discretisation error, due to the discretisation of both the mathematical model and domain, is estimated following the procedure described in Eça and Hoekstra (2014). In this procedure, the discretisation error ϵ is estimated by the equation:

$$\epsilon = \phi_i - \phi_0 = \alpha h_i^p, \tag{13}$$

in which ϕ_i stands for any integral or local flow quantity, ϕ_0 is the estimate of the exact solution, α a constant, p is the observed order of accuracy and h_i is the typical cell size of grid i, determined in our case from the total number of grid cells N_{cells} by $h_i = (1/N_{\mathrm{cells}})^{1/3}$. The unknown coefficients in Equation (13) are determined from a least-square fit of the numerical solutions on systematically refined grids. The error estimate is then converted into an numerical uncertainty U_{num} that depends on the observed order of accuracy and on the standard deviation of the fit.

The convergence of the thrust and torque coefficients with the grid refinement ratio h_i/h_1 is presented in Figure 5. The plots include also the fits for each model and Reynolds number. An apparent order of convergence between 1.17 and 1.59 is obtained for the simulations at $\mathrm{Re} = 1{\times}10^4$. For the other Reynolds number regimes, second-order convergence is achieved from the least-square fit, with the exception of the thrust coefficient predicted by the $k-\omega$ SST turbulence model at $\mathrm{Re} = 1{\times}10^7$, where an apparent order of convergence equal to 1.84 is obtained. However, not all cases show monotonic convergence. Different estimations of the exact solution are observed from the comparison between the turbulence and transition models at the Reynolds number regimes $\mathrm{Re} = 5{\times}10^5$ and $1{\times}10^7$. The estimated numerical uncertainties are the order of 0.4-4.2%. We note that the $\gamma - \tilde{\mathrm{Re}}_{\theta_t}$ transition model was not able to converge for the coarser grids at $\mathrm{Re} = 1{\times}10^7$. Finally, the variation of the open-water quantities in comparison to the finest grid is presented in Table 4, where a reduction with the increase of the number of cells is observed. For practical purposes, the grid with 17.8 million cells is chosen in the subsequent studies for the Reynolds numbers between $1{\times}10^4$ and $5{\times}10^5$, since its variation to the finest grid is lower than 1.0%. For the Reynolds numbers between $1{\times}10^6$ and $1{\times}10^7$, the grid with 11 million cells is used.

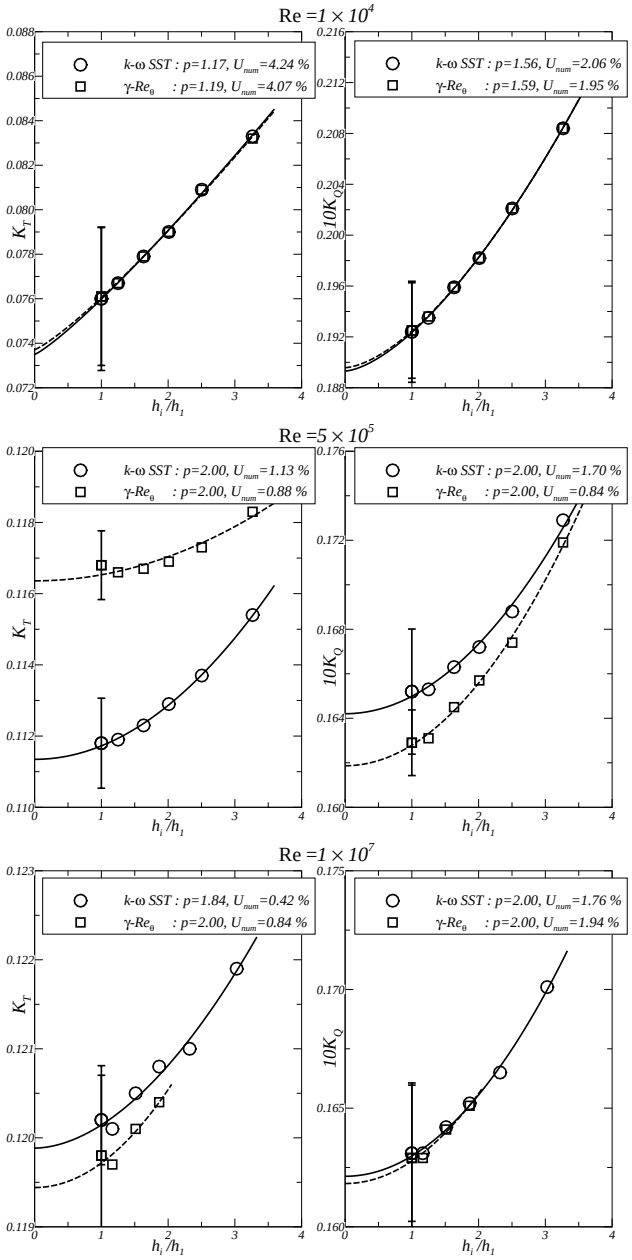

Figure 5: Convergence of K_T (left) and $10K_Q$ (right) with the grid refinement ratio h_i/h_1 at $J = 0.568$: $\mathrm{Re} = 1{\times}10^4$ (top), $5{\times}10^5$ (middle) and $1{\times}10^7$ (bottom).

4.3 Flow Analysis

In this section the propeller flow predictions at different Reynolds number regimes are analysed. Figures 6 and 7 present the limiting streamlines and skin friction distribution on the pressure and suction sides of the blade for different Reynolds numbers at $J = 0.568$, predicted by the $k-\omega$ SST turbulence model and $\gamma-\tilde{\mathrm{Re}}_{\theta_t}$ transition model, respectively. The domains of laminar and turbulent flow are identified in the figures based on the orientation of the limiting streamlines and skin friction distribution over the blade surface.

For the Reynolds number $\mathrm{Re} = 5{\times}10^5$, the numerical results are also compared with two sets of experiments carried out at MARIN with and without leading-edge roughness (LER). For the tests with LER the entire leading-edge was roughened with 60 μm carborundum grains. The paint-test photos published in Boorsma (2000) are shown in Figure 8, where laminar and turbulent flow regimes are visualised over the propeller blades. On the inner radii until $r/R = 0.5$ of the smooth propeller, laminar flow is seen until approximately 70% of the blade chord, followed by transition to turbulent flow on the pressure side and trailing-edge separation on the suction side. On the outer radii, transition occurs before the blade mid-chord. On the propeller with LER, the roughness becomes effective around $r/R = 0.5$ and turbulent flow develops from the leading-edge.

Table 4: Variation of the force coefficients with grid density compared to the finest grid at $J = 0.568$. $\mathrm{Re} = 1{\times}10^4$, $5{\times}10^5$ and $1{\times}10^7$.

	$k-\omega$ SST			$\gamma-\tilde{\mathrm{Re}}_{\theta_t}$		
Grid	ΔK_T	ΔK_Q	$\Delta\eta_0$	ΔK_T	ΔK_Q	$\Delta\eta_0$
$\mathrm{Re} = 1{\times}10^4$						
1.0M	9.6%	8.3%	1.1%	9.3%	8.3%	1.1%
2.2M	6.5%	5.0%	1.4%	6.3%	5.0%	1.4%
4.3M	4.0%	3.0%	0.8%	3.8%	3.0%	0.8%
8.0M	2.5%	1.8%	0.6%	2.4%	1.8%	0.6%
17.8M	0.0%	0.6%	0.3%	0.9%	0.6%	0.2%
$\mathrm{Re} = 5{\times}10^5$						
1.0M	3.2%	4.7%	-1.4%	1.3%	5.4%	-3.9%
2.2M	1.7%	2.2%	-0.5%	0.4%	2.8%	-2.3%
4.3M	0.9%	1.2%	-0.3%	0.1%	1.7%	-1.6%
8.0M	0.5%	0.7%	-0.2%	-0.1%	0.9%	-1.0%
17.8M	0.0%	0.1%	-0.1%	-0.2%	0.1%	-0.3%
$\mathrm{Re} = 1{\times}10^7$						
1.4M	1.4%	4.3%	-2.7%	–	–	–
3.2M	0.7%	2.1%	-1.4%	–	–	–
6.1M	0.5%	1.3%	-0.8%	0.5%	1.4%	-0.9%
11.4M	0.3%	0.7%	-0.5%	0.3%	0.8%	-0.5%
25.0M	-0.1%	0.0%	0.0%	-0.1%	0.0%	-0.2%

Since surface roughness is used to force the flow to the turbulent regime, the numerical results obtained with the $k-\omega$ SST turbulence model are compared with the paint-test from the propeller with LER. From the examination of the paint-test photos and limiting streamlines, different flow patterns are obtained at the inner radii. At the outer radii, the $k-\omega$ SST turbulence model predicts transition near the leading-edge on both sides of the propeller blade bringing the limiting streamlines to a good agreement with the streamline patterns. For the smooth propeller experiments, where natural transition is expected to occur, the numerical results obtained with the $\gamma-\tilde{\mathrm{Re}}_{\theta_t}$ transition model are compared with the paint-tests. However, due to the limitations of the $\gamma-\tilde{\mathrm{Re}}_{\theta_t}$ transition model for blind prediction

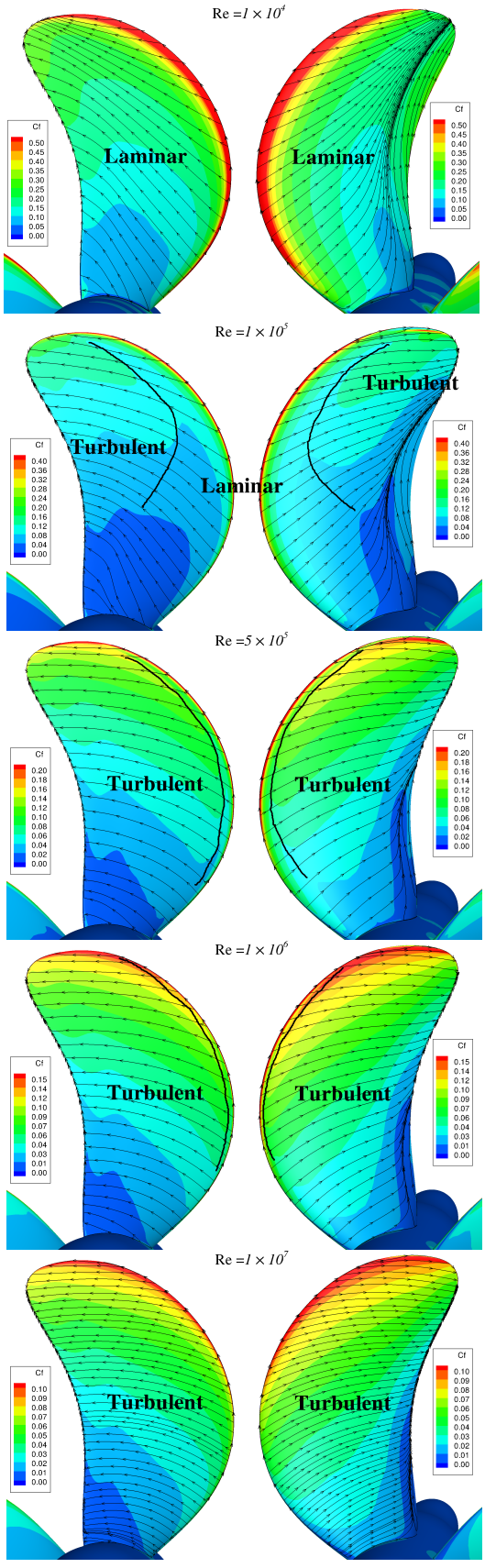

Figure 6: Limiting streamlines and skin friction coefficient using the $k-\omega$ SST turbulence model at different Reynolds numbers for $J = 0.568$. Pressure side (left) and suction side (right).

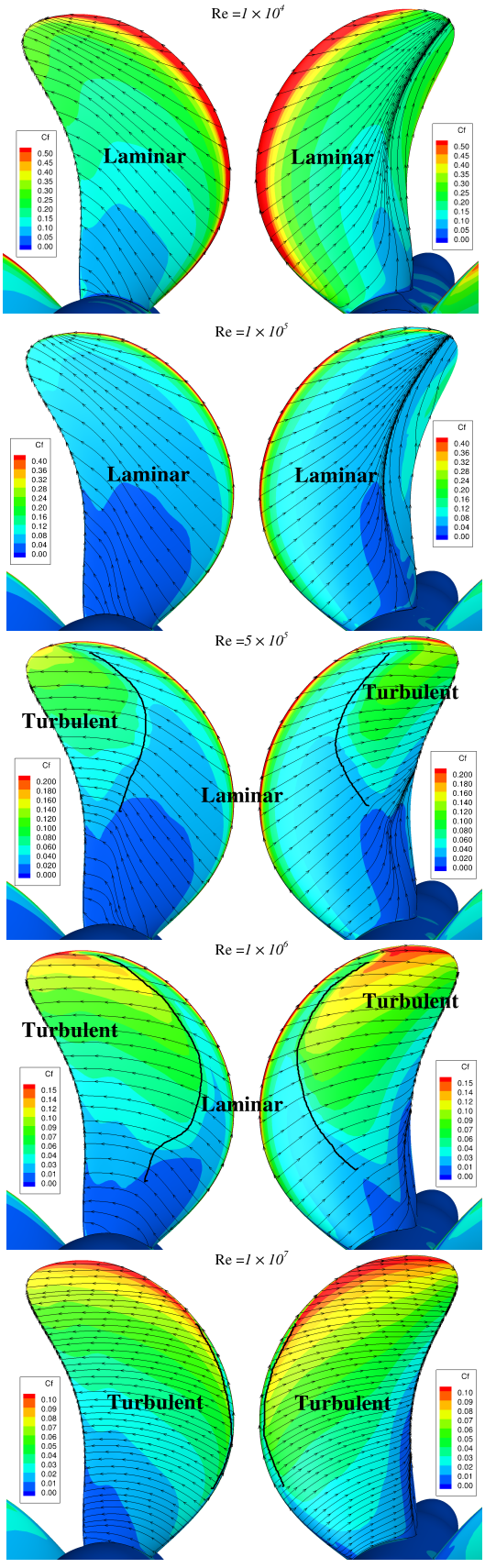

Figure 7: Limiting streamlines and skin friction coefficient using the $\gamma - \tilde{\mathrm{Re}}_{\theta_t}$ transition model at different Reynolds numbers for $J = 0.568$. Pressure side (left) and suction side (right).

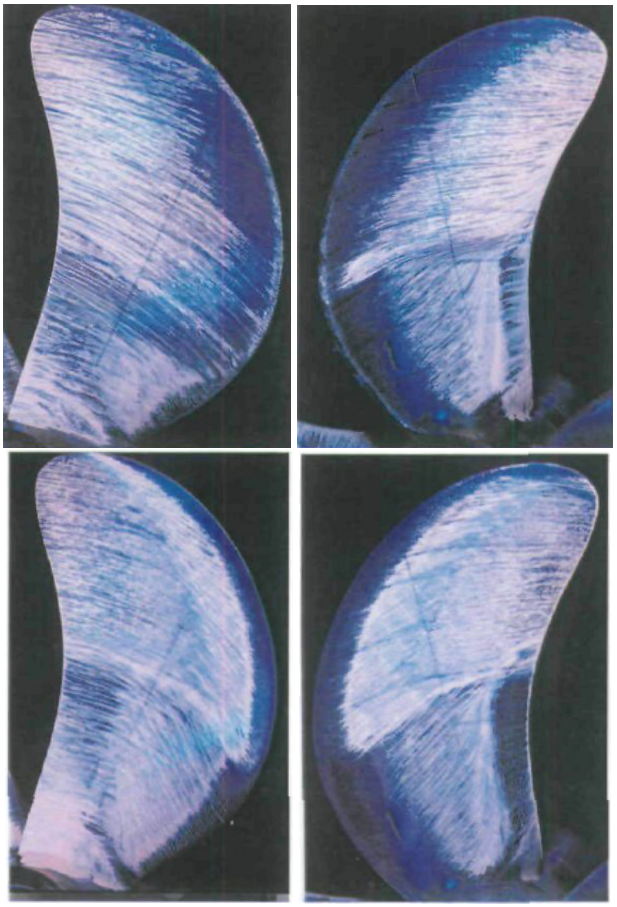

Figure 8: Propeller paint-tests with (top) and without leading-edge roughness (bottom) at $\mathrm{Re} = 5{\times}10^5$ for $J = 0.568$. Photos taken from Boorsma (2000).

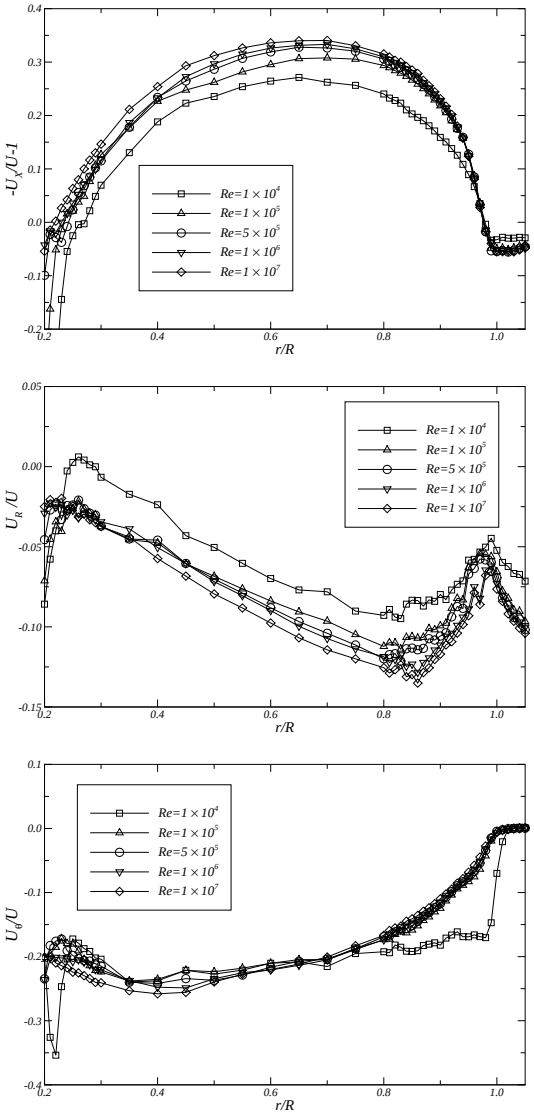

Figure 9: Circumferentially averaged velocity components at $x/R = 0.15$ for $J = 0.568$ using the $k-\omega$ SST turbulence model at different Reynolds numbers: (top) axial velocity, (middle) radial velocity and (bottom) tangential velocity.

of transitional flow, the inlet turbulence quantities were selected in a previous study, see Baltazar et al. (2018), in order to have a good agreement between the limiting streamlines and the paint-tests.

For the lower Reynolds numbers, a laminar flow regime is predicted by both models, since the limiting streamlines are more radially directed. With the increase in the Reynolds number the limiting streamlines become more circumferentially directed and the separation region near the trailing-edge reduces from the higher to the lower radii. Significant differences are seen in the blade boundary-layer flow predicted by the $k-\omega$ SST turbulence model and $\gamma - \tilde{\mathrm{Re}}_{\theta_t}$ transition model for the Reynolds numbers between $1{\times}10^5$ and $1{\times}10^6$. At these flow regimes, transition from laminar to turbulent flow occurs earlier with the $k-\omega$ SST turbulence model. For the higher Reynolds number, a turbulent flow regime over the blade surface is predicted by both models. Still, a small laminar flow region near the blade leading-edge is obtained with the $\gamma - \tilde{\mathrm{Re}}_{\theta_t}$ transition model.

In addition to the blade boundary-layer flow, the prediction of the wake flow, expecially the tip-vortex, plays an important role in the propeller performance analysis. Figures 9 and 10 present the cylindrical components of the circumferentially averaged velocity at the downstream plane $x/R = 0.15$ for $J = 0.568$, predicted by the $k-\omega$ SST turbulence model and $\gamma - \tilde{\mathrm{Re}}_{\theta_t}$ transition model, respectively. All values refer to the inertial earth-fixed reference frame and are normalised by the propeller advance speed U. The cylindrical components are defined as follows: the axial velocity U_X is positive upstream, the radial velocity U_R is positive outward, and the tangential velocity U_θ is measured opposite to the direction of propeller rotation. Results show that both models capture flow acceleration in the mid-span region. In addition, from the predicted negative radial velocities, flow contraction is obtained in the

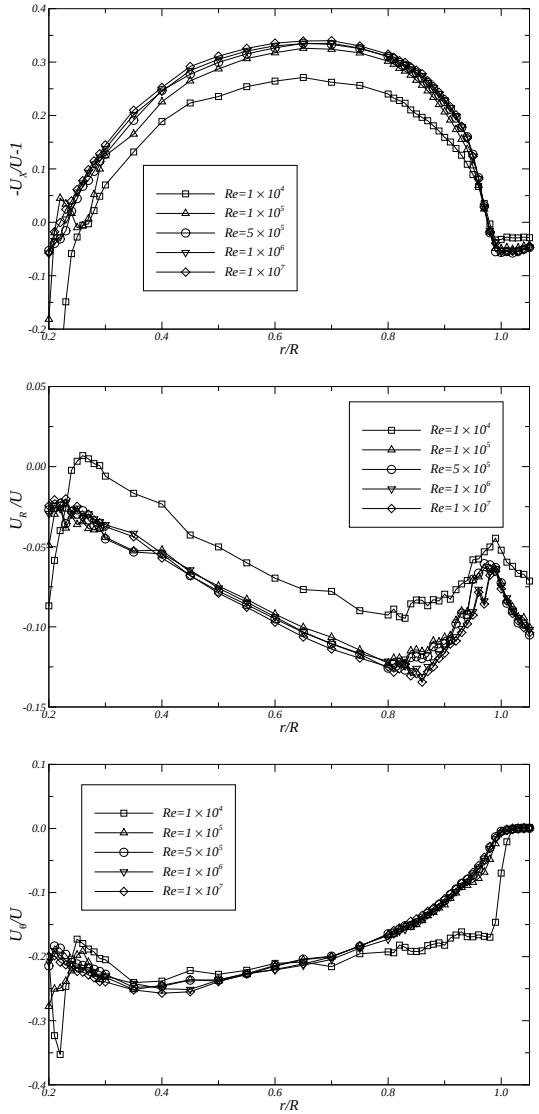

Figure 10: Circumferentially averaged velocity components at $x/R = 0.15$ for $J = 0.568$ using the $\gamma - \tilde{\mathrm{Re}}_{\theta_t}$ transition model at different Reynolds numbers: (top) axial velocity, (middle) radial velocity and (bottom) tangential velocity.

wake region. From the comparison between Figures 9 and 10, minor differences are observed between the turbulence and transition models. One major exception is observed for the axial and radial velocity components at the Reynolds number $\mathrm{Re} = 1{\times}10^5$. These differences are related to the predicted flow regimes by the $k-\omega$ SST turbulence model and $\gamma - \tilde{\mathrm{Re}}_{\theta_t}$ transition model, see Figures 6 and 7, and affect also the size of the trailing-edge flow separation region.

4.4 Performance Prediction

In this section the influence of the Reynolds number on the predicted propulsive performance is investigated. Tables 5 to 6 present the propeller thrust and torque coefficients for the various Reynolds numbers, including the pressure and friction contributions, obtained with the $k-\omega$ SST turbulence model and $\gamma - \tilde{\mathrm{Re}}_{\theta_t}$ transition model, respectively. The prediction of the scale-effects on the propeller thrust and torque compared to $\mathrm{Re} = 5{\times}10^5$ is also included.

From the results, an increase in the propeller thrust with the rising of the Reynolds number is obtained for both models. For the torque coefficient, with the exception of the lower Reynolds number ($\mathrm{Re} = 1{\times}10^4$), small variations are

Table 5: Pressure $(_p)$ and friction $(_f)$ contributions to the propeller thrust coefficient at $J = 0.568$. Prediction of the scale-effects on K_T compared to $\mathrm{Re} = 5{\times}10^5$.

Re	K_{T_p}	K_{T_f}	K_T	ΔK_T
$k-\omega$ SST				
$1{\times}10^4$	0.0839	-0.00722	0.0767	-31.5%
$5{\times}10^4$	0.0992	-0.00323	0.0960	-14.2%
$1{\times}10^5$	0.1070	-0.00290	0.1041	-7.0%
$5{\times}10^5$	0.1143	-0.00242	0.1119	–
$1{\times}10^6$	0.1171	-0.00219	0.1149	2.7%
$5{\times}10^6$	0.1209	-0.00172	0.1192	6.5%
$1{\times}10^7$	0.1221	-0.00154	0.1205	7.7%
$\gamma - \tilde{\mathrm{Re}}_{\theta_t}$				
$1{\times}10^4$	0.0839	-0.00722	0.0767	-34.2%
$5{\times}10^4$	0.0974	-0.00314	0.0942	-19.2%
$1{\times}10^5$	0.1120	-0.00215	0.1099	-5.7%
$5{\times}10^5$	0.1183	-0.00172	0.1166	–
$1{\times}10^6$	0.1193	-0.00196	0.1173	0.6%
$5{\times}10^6$	0.1207	-0.00174	0.1190	2.1%
$1{\times}10^7$	0.1217	-0.00158	0.1201	3.0%

Table 6: Pressure $(_p)$ and friction $(_f)$ contributions to the propeller torque coefficient at $J = 0.568$. Prediction of the scale-effects on K_Q compared to $\mathrm{Re} = 5{\times}10^5$.

Re	$10K_{Q_p}$	$10K_{Q_f}$	$10K_Q$	ΔK_Q
$k-\omega$ SST				
$1{\times}10^4$	0.1164	0.0772	0.1935	17.1%
$5{\times}10^4$	0.1274	0.0357	0.1632	-1.3%
$1{\times}10^5$	0.1330	0.0325	0.1655	0.1%
$5{\times}10^5$	0.1394	0.0260	0.1653	–
$1{\times}10^6$	0.1428	0.0232	0.1660	0.4%
$5{\times}10^6$	0.1468	0.0180	0.1648	-0.3%
$1{\times}10^7$	0.1481	0.0161	0.1642	-0.7%
$\gamma - \tilde{\mathrm{Re}}_{\theta_t}$				
$1{\times}10^4$	0.1164	0.0772	0.1936	18.7%
$5{\times}10^4$	0.1272	0.0344	0.1616	-0.9%
$1{\times}10^5$	0.1435	0.0240	0.1675	2.7%
$5{\times}10^5$	0.1439	0.0192	0.1631	–
$1{\times}10^6$	0.1453	0.0211	0.1664	2.0%
$5{\times}10^6$	0.1466	0.0181	0.1648	1.0%
$1{\times}10^7$	0.1477	0.0164	0.1641	0.6%

Table 7: Propeller force predictions at $\mathrm{Re} = 5{\times}10^5$ for $J = 0.568$. Comparison with experimental results (Boorsma 2000).

	K_T	$10K_Q$
$k-\omega$ SST	0.1119	0.1653
$\gamma - \tilde{\mathrm{Re}}_{\theta_t}$	0.1166	0.1631
Experimental (LER)	0.118	0.176
Experimental	0.129	0.174

found. In addition, with the increase of the Reynolds number a growth in the pressure contribution to the propeller force coefficients is observed. For the friction contribution, a decrease is obtained with the rising of the Reynolds number. However, an oscillatory behaviour is observed at $(\mathrm{Re} = 1{\times}10^5)$ for the $\gamma - \tilde{\mathrm{Re}}_{\theta_t}$ transition model. For the full-scale Reynolds number $(\mathrm{Re} = 1{\times}10^7)$, an increase in the propeller thrust of 7.7% with the $k-\omega$ SST turbulence model and of 3% with the $\gamma - \tilde{\mathrm{Re}}_{\theta_t}$ transition model compared to model-scale $(\mathrm{Re} = 5{\times}10^5)$ are obtained. For the propeller torque, small variations are observed, with 0.7% reduction for the $k-\omega$ SST turbulence model and 0.6% increase for the $\gamma - \tilde{\mathrm{Re}}_{\theta_t}$ transition model. We note that these differences are smaller than the estimated numerical uncertainty.

The different estimations of the scale-effects are influenced by the distinct propeller flow simulations obtained by the $k-\omega$ SST turbulence model and $\gamma - \tilde{\mathrm{Re}}_{\theta_t}$ transition model at model-scale $(\mathrm{Re} = 5{\times}10^5)$. The propeller force predictions at $\mathrm{Re} = 5{\times}10^5$ are compared with the experiments in Table 7. A higher thrust coefficient is obtained with the $\gamma - \tilde{\mathrm{Re}}_{\theta_t}$ transition model, similar to the experimental measurements for the smooth propeller. The relative differences for the thrust coefficient are equal to -9.6% for the $\gamma - \tilde{\mathrm{Re}}_{\theta_t}$ transition model in comparison with the smooth propeller, and -5.2% for the $k-\omega$ SST turbulence model in comparison to the propeller with LER. For the propeller torque, a minor effect due to the application of LER is seen in the experimental measurements. A similar effect is observed in the numerical predictions from both models. The relative differences for the torque coefficient are in the order of 6%.

5 SUMMARY AND CONCLUSIONS

In this paper viscous flow calculations using a RANS code are presented for a marine propeller in open-water conditions at different Reynolds numbers ranging from 10^4 to 10^7. The $\gamma - \tilde{\mathrm{Re}}_{\theta_t}$ transition model, which solves two additional equations, γ and $\tilde{\mathrm{Re}}_{\theta_t}$, for predicting flow transition is considered and results are compared to the commonly used $k-\omega$ SST turbulence model, where flow transition is taken care implicitly by the model. The results presented in this study can be summarised as follows:

- For the various Reynolds number calculations and due to the strong dependence of the $\gamma - \tilde{\mathrm{Re}}_{\theta_t}$ transition model on the inlet turbulence quantities, a relation between the inlet eddy-viscosity ratio and the Reynolds number has been found to maintain the decay rate of the turbulence quantities along the streamwise direction.

- The influence of the iterative error and discretisation error in the propeller force predictions has been studied. Results show that convergence of the intermittency γ is not obtained for the higher Reynolds numbers. Still, a negligible effect is expected on the predicted propeller forces, since global convergence is achieved for the momentum and continuity equations in all cases. The discretisation error was estimated from a procedure based on grid refinement studies. In this analysis an apparent order of convergence between 1 and 2 is observed, and the predicted numerical uncertainties are in the order of 0.4-4.2%.

- The blade boundary-layer flow and the predicted velocities in the wake region have been analysed. Different flow solutions are obtained with the $k-\omega$ SST turbulence model and $\gamma - \tilde{\mathrm{Re}}_{\theta_t}$ transition model in the range between $\mathrm{Re} = 1{\times}10^5$ and $1{\times}10^6$. At these Reynolds numbers, transition from laminar to turbulent flow occurs earlier with the $k-\omega$ SST turbulence model. As expected, a laminar flow regime is predicted by both models for lower Reynolds numbers, whereas a turbulent flow regime is obtained for higher Reynolds numbers.

- At model-scale Reynolds number $(\mathrm{Re} = 5{\times}10^5)$, the limiting streamlines have been compared with paint flow tests for the propeller with and without LER. The limiting streamlines produced by the $k-\omega$ SST turbulence model agree well on the outer part of the rough propeller. For the smooth propeller, the inlet turbulence quantities of the $\gamma - \tilde{\mathrm{Re}}_{\theta_t}$ transition model were selected to match the paint-tests.

- The propulsive predictions produced by the $k-\omega$ SST turbulence model and $\gamma - \tilde{\mathrm{Re}}_{\theta_t}$ transition model near the design operating point show an increase in the thrust coefficient for rising Reynolds number. For the torque coefficient, with the exception of the lower Reynolds number $(\mathrm{Re} = 1{\times}10^4)$, small variations are achieved. These variations result in an increase of the open-water efficiency between model- and full-scale. Compared to the model-scale Reynolds number $(\mathrm{Re} = 5{\times}10^5)$, an increase in the thrust coefficient of 7.7% and 3.0% is obtained with the $k-\omega$ SST turbulence model and $\gamma - \tilde{\mathrm{Re}}_{\theta_t}$ transition model, respectively.

6 ACKNOWLEDGMENTS

The authors acknowledge the Laboratory for Advanced Computing at University of Coimbra (www.lca.uc.pt) for providing computing resources that have contributed to part of the results reported in this paper. We are indebted to Guilherme Vaz, Rui Lopes and Daniela Melo for the fruitful discussions on this topic.

REFERENCES

Abdel-Maksoud, M. and Heinke, H.-J. (2002). 'Scale effects on ducted propellers'. In Proceedings of the 24th ONR Symposium on Naval Hydrodynamics, Kukuoka, Japan.

Baltazar, J., Rijpkema, D., and Falcão de Campos, J. A. C. (2018). 'On the Use of the γ-$\tilde{\mathrm{Re}}_{\theta_t}$ Transition Model for the Prediction of the Propeller Performance at Model-Scale'. Ocean Engineering, 170:6 – 19.

Bhattacharyya, A., Krasilnikov, V., and Steen, S. (2016). 'Scale Effects on Open Water Characteristics of a Controllable Pitch Propeller Working Within Different Duct Designs'. Ocean Engineering, 112:226 – 242.

Boorsma, A. (2000). Improving Full Scale Ship Powering Performance Predictions by Application of Propeller Leading Edge Roughness, Part 1: Effect of Leading Edge Roughness on Propeller Performance. Master's thesis, University of Technology Delft.

Eça, L. and Hoekstra, M. (2008). 'The Numerical Friction Line'. Journal of Marine Science and Technology, 13(4):328 – 345.

Eça, L. and Hoekstra, M. (2014). 'A Procedure for the Estimation of the Numerical Uncertainty of CFD Calculations Based on Grid Refinement Studies'. Journal of Computational Physics, 262:104 – 130.

Eça, L., Lopes, R., Vaz, G., Baltazar, J., and Rijpkema, D. (2016). 'Validation exercises of mathematical models for the prediction of transitional flows'. In Proceedings of the 31st Symposium on Naval Hydrodynamics, Monterey, California, USA.

International Towing Tank Conference (2017). '1978 ITTC performance prediction method'. Technical Report ITTC - Recommended Procedures and Guidelines 7.5-02-03-01.4, Revision 07.

Jones, W. and Launder, B. (1972). 'The Prediction of Laminarization with a Two-Equation Model of Turbulence'. International Journal of Heat and Mass Transfer, 15(2):301 – 314.

Jonk, A. and Willemsen, H. (1994). 'Calm water model tests for a 300,000 DWT crude oil carrier'. Technical Report 012383-1-VT, MARIN.

Krasilnikov, V., Sun, J., and Halse, K. (2009). 'CFD investigation in scale effects on propellers with different magnitude of skew in turbulent flow'. In Proceedings of the First International Symposium on Marine Propulsors, Trondheim, Norway.

Langtry, R. and Menter, F. (2009). 'Correlation-Based Transition Modeling for Unstructured parallelized Computational Fluid Dynamics Codes'. AIAA Journal, 47(12):2894 – 2906.

Menter, F. (1994). 'Two-Equation Eddy-Viscosity Turbulence Models for Engineering Applications'. AIAA Journal, 32(8):1598 – 1605.

Menter, F., Kuntz, M., and Langtry, R. (2003). 'Ten years of industrial experience with the SST turbulence model'. In Proceedings of the Fourth International Symposium on Turbulence, Heat and Mass Transfer, Antalya, Turkey.

Oberkampf, W. and Roy, C. (2010). 'Verification and Validation in Scientific Computing'. Cambridge University Press.

Rijpkema, D., Baltazar, J., and Falcão de Campos, J. A. C. (2015). 'Viscous flow simulations of propellers in different Reynolds number regimes'. In Proceedings of the Fourth International Symposium on Marine Propulsors, Austin, Texas, USA.

Rijpkema, D. and Vaz, G. (2011). 'Viscous flow computations on propulsors: verification, validation and scale effects'. In Proceedings of the International Conference on Developments in Marine CFD, London, UK.

Sánchez-Caja, A., González-Adalid, J., Pérez-Sobrino, M., and Sipilä, T. (2014). 'Scale Effects on Tip Loaded Propeller Performance Using a RANSE Solver'. Ocean Engineering, 88:607 – 617.

Schmitt, F. (2007). 'About Boussinesq's Turbulent Viscosity Hypothesis: Historical Remarks and a Direct Evaluation of its Validity'. Comptes Rendus Mécanique, 335(9 - 10):617 – 627.

Spalart, P. and Rumsey, C. (2007). 'Effective Inflow Conditions for Turbulence Models in Aerodynamic Calculations'. AIAA Journal, 45(10):2544 – 2553.

Stanier, M. (1998). 'The application of RANS code to investigate propeller scale effects'. In Proceedings of the 22th ONR Symposium on Naval Hydrodynamics, Washington, DC, USA.

Wilcox, D. (1988). 'Reassessment of the Scale-Determining Equation for Advanced Turbulence Models'. AIAA Journal, 26(11):1299 – 1310.